Journal of
Materials Chemistry C

ROYAL SOCIETY OF CHEMISTRY

PAPER

View Article Online
View Journal

Cite this: DOI: 10.1039/d5tc02216a

Enhancement of built-in electric field strength of BiOCl/NMT Z-scheme heterojunctions through photoinitiated defects for optimized photocatalytic performance†

Libo Wang, *[ac] Xiayu Wu,[a] Yangyang Zhang,[a] Yitong Wang,[a] Qiguo Zhu,[a] Ya Wang,[ac] Jingyao Li,[ac] Gang Liu*[ac] and Zhenhua Hou*[b]

Received 8th June 2025,
Accepted 10th July 2025

DOI: 10.1039/d5tc02216a

rsc.li/materials-c

Facilitating carrier migration within Z-scheme heterojunctions is essential for improving the efficiency of photocatalytic nitrogen fixation. Herein, we successfully constructed BiOCl/NMT Z-scheme heterojunctions by a simple solvothermal process and adsorption–deposition methods. Under photoinitiation, BiOCl quantum dots could be transformed into defective structures with more oxygen vacancies. Increasing the concentration of oxygen vacancies in BiOCl not only altered the energy band structure, but also further modulated the position of the Fermi energy level (E_f). The downward migration of the E_f of BiOCl enhanced the built-in electric field (BEF) strength between it and NMT, which enabled the rapid separation and migration of photogenerated carriers. 0.05-BiOCl/NMT expressed optimal nitrogen reduction performance along with NH_3 generation at a rate of 88.6 μmol g^{-1} h^{-1}. The nitrogen fixation rate of 0.05-BiOCl/NMT was 8.5 and 2.7 times higher than that of BiOCl and NMT. This work adjusted the BEF intensity by a straightforward self-conversion to a defective structure, which offered fresh insights into the promotion of carrier separation in photocatalytic nitrogen fixation.

1. Introduction

Global ammonia (NH_3) consumption is about 180 million tons per year.[1] The increasing demand for ammonia is attributed to the rapid development of the fertilizer, chemical and metallurgical industries.[2] As a relatively stable noble gas, nitrogen has an $N \equiv N$ triple bond with an energy of 941.69 kJ mol^{-1}. Industrial ammonia synthesis (Haber–Bosch process) requires the reduction of N_2 with the assistance of energy provided by fossil fuels.[3] Accompanied by increased awareness of environmental protection and continuous technological innovation, ammonia synthesis is gradually transforming from high energy consumption and high emission to green and low carbon.[4] Renewable energy-driven nitrogen fixation reactions have attracted extensive attention. Electrocatalytic nitrogen fixation and photoelectrocatalytic nitrogen fixation have high energy requirements, and the voltage and current need to be precisely regulated.[5] In contrast, photocatalytic ammonia synthesis utilizes solar energy as a driving force, which allows for the activation and fixation of N_2 at ambient temperature and pressure.[6] Photocatalytic nitrogen fixation is considered an advanced technology that is sustainable and harmless to the environment.[7] The method utilizes renewable solar energy to react N_2 and H_2O under mild conditions. Complex high-pressure reaction units are not required for photocatalytic nitrogen fixation, and equipment investment and operating costs are reduced.[8] However, photocatalytic ammonia synthesis still suffers from the issue of low yield. Researchers modified the catalysts to address the thermodynamic and kinetic challenges, such as extending the light absorption range, increasing the active sites and promoting carrier migration.[9]

NH_2-MIL-125(Ti) (NMT), as a typical Ti-based metal–organic framework (MOF) material, has received wide interest in the field of photocatalytic nitrogen fixation due to its distinct structural and functional properties.[10] Unlike other MOFs, NMT remains chemically and structurally stable in aqueous environments.[11] NMT exhibits excellent porous and specific surface area properties, and it shows excellent performance in light absorption and reactant adsorption.[12] The amino group ($-NH_2$) is positively charged, which is able to change the surface electronic structure of NMT.[13] The localized electronic states

---

[a] *Institute of Chemical & Industrial Bio-engineering, Jilin Engineering Normal University, Changchun, Jilin 130052, China. E-mail: wanglb733@nenu.edu.cn, 67297220@qq.com*

[b] *Institute of Mechanical and Vehicle Engineering, Changchun University, Changchun, Jilin 130022, China. E-mail: houzhenhua19930520@163.com*

[c] *Jilin Science and Technology Innovation Center of Green Synthesis and New Materials Research and Development, Changchun, Jilin 130052, China*

† Electronic supplementary information (ESI) available: XRD, SEM, electrochemical impedance spectroscopy and NH_3 generation rate in different free radical scavengers. See DOI: **https://doi.org/10.1039/d5tc02216a**

generated by $-NH_2$ can effectively reduce the recombination rate of carriers.[14] The metal node Ti^{4+} can act as an active site for photocatalysis attributed to the abundance of unoccupied d orbitals, which can accept electrons for valence changes.[15] However, the NMT monomer lacks active sites and shows a high electron–hole complexation rate.

The fabricated heterojunction is capable of forming a BEF in the catalysis, which drives the carriers to undergo rapid separation without any external energy consumption.[16] In general, the strength of the BEF is an important driving force that affects the interfacial charge migration properties. In order to break the bottleneck of the slow carrier migration rate in heterojunction type catalysts, several measures have been undertaken to increase the strength of the BEF. Lan *et al.* modulated the intensity of the BEF at the MOF/COF heterojunction interface by changing the exposed crystalline surface of MOFs.[17] The elevated space charge separation in the heterojunction realized an efficient photocatalytic reaction. Jiang *et al.* precisely controlled the content of oxygen vacancies in WO_{3-x}, which enabled the construction of the NH_2-MIL-125-Ti/WO_{3-x} heterojunction with a strong charge driving force to accelerate the carrier transfer kinetics.[18] The bandgap properties can be tuned by oxygen vacancy (OV) engineering, and this approach is considered to be a more efficient and economical strategy for modulating the BEF strength at heterojunction interfaces. The OVs have a low formation energy, which allows them to be the most commonly researched anionic defects.[19] The presence of OVs increases the electron density around the defective structure, and the ability of the catalyst to adsorb reactants is significantly increased.[20] Therefore, the construction of heterojunctions between NMT and semiconductors with precisely tunable concentrations of OVs is an attractive method for designing highly active catalysts.

BiOCl has been widely emphasized in the research in the field of photocatalysis. The structure of BiOCl consists of alternating stacked $[Bi_2O_2]^{2+}$ layers and double Cl^- layers.[21] The unique interlayer structure generates an electric field inside BiOCl, which facilitates the separation of photogenerated carriers.[22] Moreover, researchers noticed that the color of BiOCl shifts to grey after irradiation with UV spectra, which may be attributed to the generation of OVs on the surface of BiOCl.[23] The release of oxygen atoms from the BiOCl surface results in special electronic properties and carrier separation. The OVs in BiOCl possess tunability, and the positions of their E_f are changed. Modifying the E_f positions of different components in heterojunction catalysts effectively modulates the BEF strength.[18] Elevating the BEF can provide a powerful internal driving force to accelerate electron and hole migration between semiconductor interfaces.[24] Consequently, altering the content of OVs in BiOCl to adjust the E_f position is a feasible strategy to elevate the BEF.

In this work, we immobilized BiOCl quantum dots on the NMT surface (BiOCl/NMT) by an adsorption–deposition method. Under photoinitiation, the concentration of OVs in BiOCl increased and its Fermi energy level migrated downward. Moreover, additional OVs in BiOCl could promote the adsorption of reactants by the catalyst and store photogenerated electrons to inhibit electron–hole recombination. Signal peaks associated with DMPO–$^{\bullet}O_2^-$ and DMPO–$^{\bullet}$OH appeared in 0.05-BiOCl/NMT. The intensity of the signal peaks significantly increased with the prolongation of light irradiation. The NH_3 production rate of 0.05-BiOCl/NMT was 88.6 μmol g^{-1} h^{-1}, and the nitrogen fixation rates were 8.5 and 2.7 times higher than those of BiOCl and NMT, respectively. The enhancement of BiOCl/NMT catalytic activity was intimately related to three factors: (i) a large contact area at the BiOCl/NMT heterojunction interface provided transfer channels and abundant active sites for carrier separation; (ii) enhancement of the BEF between BiOCl and NMT contributed to the carrier separation and migration; and (iii) the Z-scheme heterojunction raised the light energy utilization and electron–hole pair redox capacity of BiOCl/NMT. This study presents a new route to enhancing the efficient photocatalytic nitrogen fixation performance of Z-scheme heterojunctions.

2. Experimental

2.1 Preparation of NMT

NMT was prepared with reference to the literature.[25] 1.086 g of the organic ligand 2-aminoterephthalic acid was weighed and dissolved in a mixed solution, the solution consisted of 18 mL of *N*,*N*-dimethylformamide (DMF) and 2 mL of methanol. The solid–liquid mixture was stirred thoroughly to ensure that the solids were completely dissolved in the solution. 0.52 mL of tetrabutyl titanate was continued to be added to the mixture. After stirring for 30 min, the obtained mixture was transferred to a 100 mL Teflon-lined stainless steel autoclave and heated at 150 °C for 20 h. After cooling, the collected solid product was washed with DMF and methanol. Further drying was carried out to obtain NMT powder.

2.2 Preparation of BiOCl

3 mmol of KCl was dissolved in 22 mL of pure water to prepare solution A. Solution B was acquired by adding 3 mmol of $Bi(NO_3)_3\cdot 5H_2O$ in 22 mL of ethylene glycol ($(CH_2OH)_2$). Solution B was mixed with solution A. The mixed solution was stirred continuously for 3.5 h. The solid product was collected by centrifugation. The collected solid product was washed with deionized water and ethanol to remove residual impurities. The white powder BiOCl was collected after drying in an oven for 6 h.

2.3 Preparation of BiOCl/NMT

An adsorption–deposition method was employed to prepare BiOCl/NMT complexes. 100 mg of NMT and an amount of KCl were put into 22 mL of pure water. $Bi(NO_3)_3\cdot 5H_2O$ was dissolved in 22 mL of $(CH_2OH)_2$. The above two solutions were mixed and stirred for 3.5 h. The collected solid catalyst was washed several times with deionized water and ethanol and dried in an oven. Based on the theoretical mass percentage of BiOCl, the samples were named 0.01, 0.05, and 0.10-BiOCl/NMT.

2.4 Preparation of A-BiOCl and A-BiOCl/NMT

The properties of BiOCl upon light irradiation were studied to illustrate that the concentration of OVs could be altered. The synthesized catalysts BiOCl and BiOCl/NMT were used to simulate the photocatalytic nitrogen fixation process. After the photocatalytic nitrogen fixation, the catalyst was collected from the reaction solution and vacuum-dried. The obtained solids were labeled as A-BiOCl and A-BiOCl/NMT, respectively.

2.5 Photocatalytic nitrogen fixation experiments

Nitrogen fixation activity was investigated in a photocatalytic reactor made of quartz. The prepared photocatalyst (0.05 g) and pure water (100 mL) were added to the reaction device. No sacrificial reagent was introduced into the catalytic solution. The reaction device was placed in ultrasonic equipment to fully disperse the catalyst in the water. High purity N_2 was continuously passed into the device under light-free conditions. After 30 min, the photocatalytic nitrogen fixation experiment was simulated using the light produced by a 300 W xenon lamp as a light source. Circulating water was injected into the periphery of the catalytic unit to maintain a constant temperature during the reaction. The rate of ammonia production was analyzed utilizing the indophenol blue method.[26]

3. Results and discussion

A series of BiOCl/NMT were produced by the adsorption–deposition method, where BiOCl quantum dots were attached to the outer surface of NMT, as shown in Scheme 1. Under light energy excitation, changes in the concentration of OVs in BiOCl were able to modify the BEF intensity between BiOCl and NMT. In Fig. 1a, the X-ray diffraction (XRD) spectrum of BiOCl classified as a tetragonal phase with a JCPDS card no. of 06-249.[27] The signal peak positions of A-BiOCl were almost identical to those of the original BiOCl. However, the intensity of the diffraction peaks became weaker. In the NMT spectra (Fig. 1b), the diffraction peaks corresponding to (101), (200), (211), (222) and (312) facets were located at 6.8°, 9.8°, 11.8°, 16.7° and 17.9°, respectively.[28] In the three composite catalysts synthesized, the intensity of the signal peaks associated with NMT gradually diminished with the increase in the content of BiOCl quantum dots. After the attachment of BiOCl to the NMT surface, the positions of diffraction peaks in the spectra of 0.01-BiOCl/NMT and 0.05-BiOCl/NMT almost coincided with those of NMT. When the loading of BiOCl was further increased, the signal peaks at 32.6° and 33.5° in the 0.10-BiOCl/NMT spectra corresponded to the (110) and (102) facets of BiOCl. By analyzing the XRD data, we understand that BiOCl was successfully attached to the NMT surface.

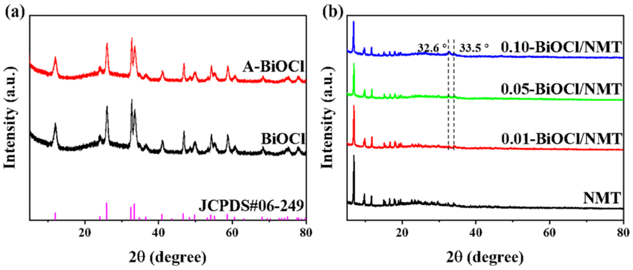

Fig. 1 The XRD patterns of (a) BiOCl and A-BiOCl, and (b) NMT and BiOCl/NMT.

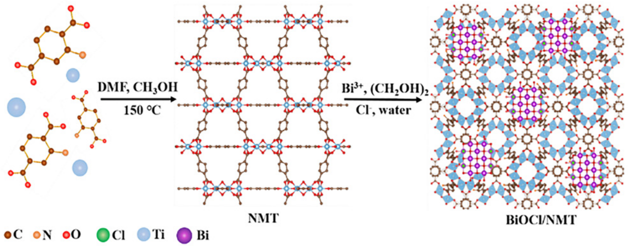

Scheme 1 Schematic illustration of BiOCl/NMT by an adsorption–deposition method.

The vibrations of each functional group in the Fourier transform infrared (FT-IR) spectroscopy spectra were utilized to further deduce the structural features of the prepared samples. In the spectrum of BiOCl (Fig. 2a), the stretching vibration of the Bi–O bond appeared at 522 cm^{-1}, and the signal peaks generated in the range of 1000–1500 cm^{-1} were attributed to the Bi–Cl bond.[29] The water adsorbed on the surface of BiOCl contained O–H functional groups, which produced the peak of the stretching vibration emerging at 1625 cm^{-1}. The intensity of the stretching peaks induced by O–H in the spectra of A-BiOCl was increased. The presence of OVs promoted the adsorption of BiOCl to water, which was consistent with the results previously reported in the literature.[30] In the NMT spectra (Fig. 2b), the stretching vibrations of the O–Ti–O bond occurred in the short wavenumber between 400 and 800 cm^{-1}.[31] The vibrational peaks appearing at 1384 and 1537 cm^{-1} were assigned to the O–C–O and C=O stretching vibrations in the carboxyl group.[32] The large band stretching vibrational peak at 3400 cm^{-1} was caused by water molecules or organic solvents trapped in the pore. In the spectra of BiOCl/NMT, the positions of the signal peaks remained essentially the same as those of NMT. However, it could be observed that the signal peak located at 1042 cm^{-1} became stronger with the increase of BiOCl loading. This might be related to the increase of Bi–Cl bonds in the complex samples. The test results of the FT-IR spectrum likewise demonstrated the synthesis of the target catalyst BiOCl/NMT.

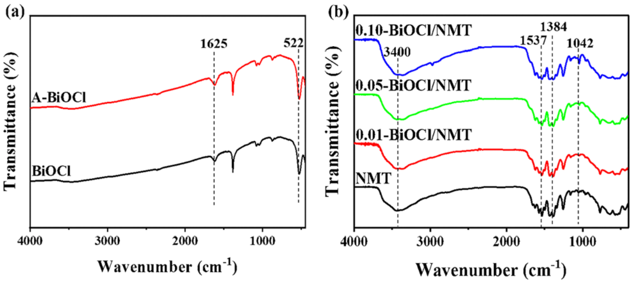

Fig. 2 FT-IR of (a) BiOCl and A-BiOCl, and (b) NMT and BiOCl/NMT.

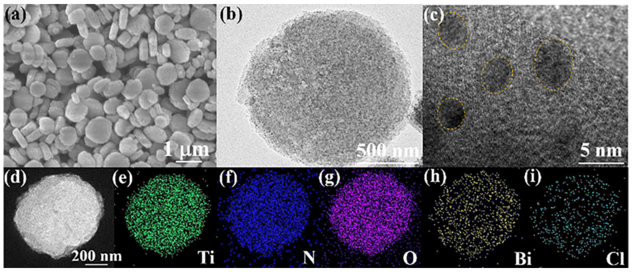

Fig. 3 (a) SEM and (b) and (c) TEM images of 0.05-BiOCl/NMT, and (d)–(i) elemental mapping of 0.05-BiOCl/NMT.

Scanning electron microscopy (SEM) was utilized to observe the microstructure and morphology of NMT and BiOCl/NMT, as shown in Fig. S1, S2 (ESI†) and Fig. 3a. NMT was typical of a disk-like structure, with a particle size distribution between 300 and 1100 nm. The particle size distribution of NMT is shown in Fig. S1b (ESI†). After BiOCl deposition, BiOCl/NMT still exhibited a disk-like structure. Due to the small size of the BiOCl quantum dots, it was not possible to observe any changes produced on the surface of the NMT from the SEM images. This information implied that the BiOCl quantum dots were uniformly attached to the NMT surface. In order to understand more precisely the size of quantum dots in BiOCl/NMT, the characteristics of the sample was investigated using transmission electron microscopy (TEM). In Fig. 3b, BiOCl nanoparticles were highly distributed on the NMT surface, and the average size of BiOCl quantum dots was approximately between 3 and 5 nm. The elemental distribution mapping of BiOCl/NMT revealed that N, O, Ti, Bi and Cl were uniformly dispersed throughout the sample.

The surface elemental composition and chemical valence of catalyst BiOCl/NMT were analyzed by X-ray photoelectron spectroscopy (XPS) testing. In Fig. S3 (ESI†), the elements C, N, O, and Ti appeared in the survey spectra of NMT. In the survey spectrum of BiOCl/NMT, signal peaks of Bi and Cl emerged in addition to those of the above elements. As shown in Fig. 4a, the high-resolution spectrum of Ti 2p contained Ti $2p_{1/2}$ and Ti $2p_{3/2}$ signal peaks. The Ti $2p_{1/2}$ and Ti $2p_{3/2}$ in NMT located at 463.1 and 457.1 eV, while the binding energies of the corresponding signal peaks in NMT/BiOCl were 463.2 and 457.3 eV, respectively. As shown in Fig. 4b, the peaks with binding energies positioned at 400.2 and 397.6 eV were classified as $-NH_2$ and C–N in the NMT spectra. In the N 1s spectra of BiOCl/NMT, the signal peaks of $-NH_2$ and C–N were observed at 400.6 and 397.9 eV. In contrast to pure NMT, the locations of both Ti 2p and N 1s in NMT/BiOCl exhibited a slight shift toward higher binding energies. In Fig. 4c, three signal peaks emerged in the high-resolution O 1s spectra of BiOCl/NMT, and correspond to C═O, defective oxygen and Ti–O/lattice O, respectively. The peak positions were located at 531.6, 530.3, and 529.5 eV. The calculation revealed that the defective oxygen accounted for 29.1% of the peak area. In Fig. 4d, the two peaks displayed in the Bi 4f spectrum of BiOCl/NMT were located at 163.3 and 158.0 eV, which were attributed to Bi $4f_{5/2}$ and Bi $4f_{7/2}$. In the spectrum of Cl 2p (Fig. S4, ESI†), two signal peaks at 200.5 and 198.7 eV were assigned to Cl $2p_{3/2}$ and Cl $2p_{5/2}$, respectively. The analysis of the XPS results indicated a strong interaction of electrons between BiOCl and NMT, and the electrons tend to transfer from NMT to BiOCl.[33]

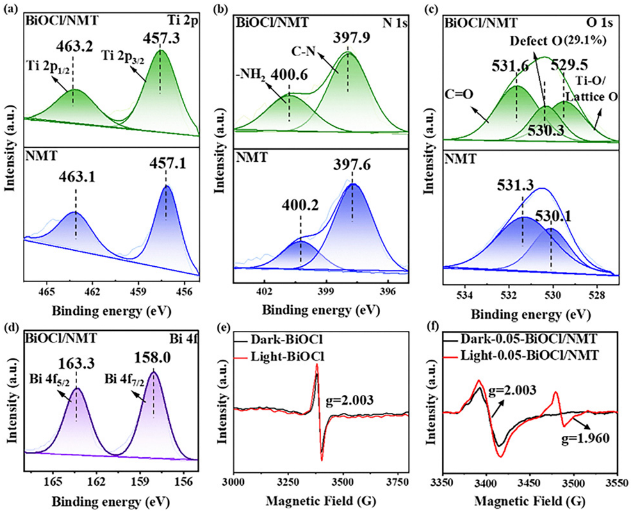

Fig. 4 (a)–(c) High resolution XPS of Ti 2p, N 1s, O 1s for 0.05-BiOCl/NMT and NMT; (d) high resolution XPS of Bi 4f for 0.05-BiOCl/NMT; and (e) and (f) ESR spectra of BiOCl and 0.05-BiOCl/NMT under light and dark conditions.

To illustrate that BiOCl quantum dots would generate more OVs under light radiation, we selected electron spin resonance (ESR) to understand the content of OVs in BiOCl under dark and light radiation conditions. As shown in Fig. 4e, the strong signal peak at $g = 2.003$ in the plot was assigned to OVs. The signal peak of BiOCl was stronger under light radiation conditions than under dark conditions, indicating the formation of new OVs on the surface of BiOCl after photoinitiation. Moreover, BiOCl quantum dots could generate additional OVs through light energy initiation. The ESR test spectra of 0.05-BiOCl/NMT under dark and light conditions are presented in Fig. 4f. The signal peak of light-0.05-BiOCl/NMT was stronger than that of dark-0.05-BiOCl/NMT, and the defective structures of BiOCl in the heterojunction catalysts were similarly generated upon photoinitiation. Light energy irradiation adjusted the concentration of OVs in BiOCl to break the scaling relationships, which facilitated the reduction of energy barriers in the photocatalytic nitrogen fixation reaction.[34] In addition, a new signal peak at $g = 1.960$ appeared in the spectrum of light-0.05-BiOCl/NMT. The generated signal peak originated from the formation of Ti^{3+}, which had unpaired electrons in its atomic orbitals. The formation of structural defects on the BiOCl surface and the synergistic effect produced by the low valence metal cations in NMT could inhibit the complexation of photogenerated electrons and holes. In Fig S5 (ESI†), the signal peak intensity of OVs in BiOCl/NMT was enhanced with increasing BiOCl loading.

The surface characteristics of the prepared catalysts were detected *via* N_2 adsorption–desorption isotherms and pore size

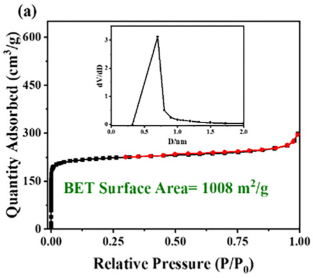

Fig. 5 (a) and (b) N_2 adsorption–desorption isotherm and pore size distribution of NMT and 0.05-BiOCl/NMT.

distribution profiles. The test results are presented in Fig. 5. NMT, as a representative porous material, had a Brunauer–Emmett–Teller (BET) surface area of 1008 m^2 g^{-1}. The N_2 adsorption–desorption isotherm of NMT exhibited a type I shape. Micropores would naturally form during the self-assembly of metal clusters with organic ligands into NMT. In the pore size distribution graph, it was similarly noticed that the pores in NMT mainly manifested as micropores. Micropores in NMT could provide large specific surface area and abundant active sites contributing to the separation of electrons and holes.[35] The BET surface area of BiOCl/NMT was 1152 m^2 g^{-1}, which was an improvement compared with NMT. This variation could be attributed to the presence of a certain amount of OVs in BiOCl quantum dots. In general, ultra-small size structures would induce defects on the catalyst surface.[36] The loading of BiOCl quantum dots on the NMT surface promoted the adsorption performance of the catalyst for N_2. The pore size in BiOCl/NMT did not change and remained microporous. Therefore, we could optimize the adsorption performance of NMT on reactants by loading of BiOCl quantum dots.

UV-vis diffuse reflectance spectroscopy (DRS) investigated the light absorption properties of all prepared samples. In Fig. 6a, the light absorption boundaries of BiOCl and A-BiOCl were quite close in the test spectra. A-BiOCl had trailing after the light absorption boundary, and A-BiOCl could utilize visible light to some extent. After the photocatalytic reaction, the band gap energy of BiOCl was reduced, and this might be related to the fact that the OVs altered the local electronic state of BiOCl.[37] After loading BiOCl on the NMT surface (Fig. 6b and Fig. S6, ESI†), the light absorption range was further shifted towards longer wavelengths. Ultra-small size BiOCl quantum dot structures evoked the creation of defective structures on their surfaces. The absorption boundary of 0.05-BiOCl/NMT reached 623 nm compared to 540 nm for NMT. The absorption edge of A-0.05-BiOCl/NMT was further red-shifted. This indicated that more OVs were produced in A-0.05-BiOCl/NMT, which enhanced the light energy utilization of the sample. The band gap energy of the samples was investigated for estimation of the DRS data using the Kubelka–Munk formula.[38] As shown in Fig. S7 (ESI†), the band gap energies of A-BiOCl and NMT were 3.04 and 2.61 eV, respectively. Increasing the concentration of OVs in BiOCl by photoinitiation altered the energy band structure. The expansion of the light absorption region of BiOCl/NMT greatly facilitated the utilization of solar energy.

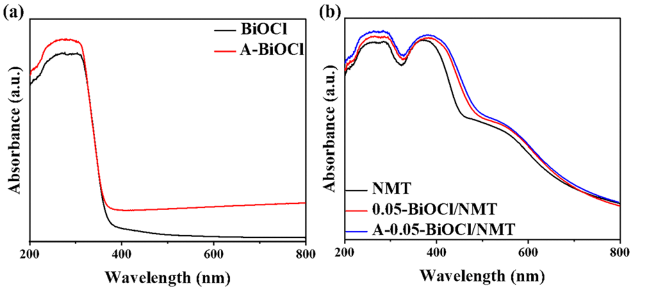

Fig. 6 UV-Vis spectra of (a) BiOCl and A-BiOCl, and (b) NMT, 0.05-BiOCl/NMT and A-0.05-BiOCl/NMT.

In order to clarify the complete energy band structure information of the synthesized samples, the positions of the conduction bands (CB) were determined through the Mott–Schottky plot. In Fig. 7a, the flat band potential value for NMT was −0.79 V. A saturated calomel electrode (SCE) was employed as a reference electrode during the test. After conversion to a standard hydrogen electrode (SHE), the corresponding flat band potential was −0.55 V. Based on the positive slope of the straight line segment of the Mott–Schottky curve within the passivation region, it was determined that NMT was an n-type semiconductor. Typically, the CB of an n-type semiconductor would be 0.1 V more negative than the flat band potential. Ultimately, the CB for NMT was established to be −0.65 V. We tracked the valence band (VB) values of A-BiOCl using ultraviolet photoelectron spectroscopy (UPS). As shown in Fig. 7b, the VB of A-BiOCl was 2.83 V. The relationship between CB, VB and band gap energy (E_g) was expressed as follows: $E_{(VB)} = E_{(Eg)} + E_{(CB)}$. The VB value for NMT was evaluated as 1.96 V, and the CB value of A-BiOCl was determined to be −0.21 V.

The separation of photogenerated carriers was analyzed with the utilization of photocurrent and steady-state photoluminescence (PL) tests. As shown in Fig. 8a, BiOCl/NMT possessed higher photocurrent densities compared to pure BiOCl and NMT. 0.05-BiOCl/NMT had approximately 3.3 and 4.2 times the photocurrent densities of BiOCl and NMT. The photocurrent intensity was high for all BiOCl/NMTs, indicating that light energy could be efficiently translated into free electrons and holes on BiOCl/NMTs. Under the initiation of light energy, more photogenerated electrons were aggregated on the surface of BiOCl/NMT. The construction of heterojunction type catalysts

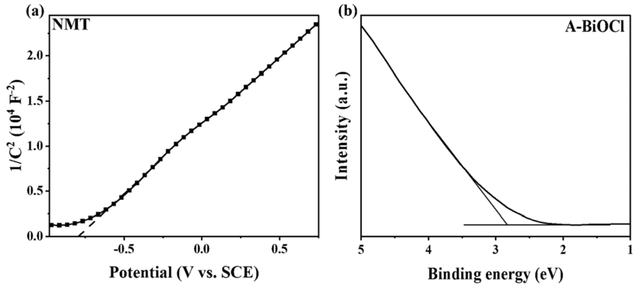

Fig. 7 (a) Mott–Schottky spectra of NMT and (b) UPS spectra of A-BiOCl.

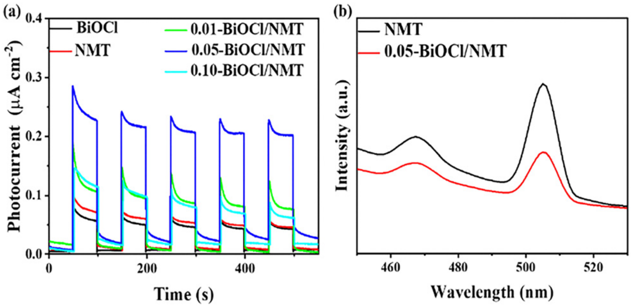

Fig. 8 (a) Photocurrent of BiOCl, NMT and BiOCl/NMT, and (b) PL of NMT and 0.05- BiOCl/NMT.

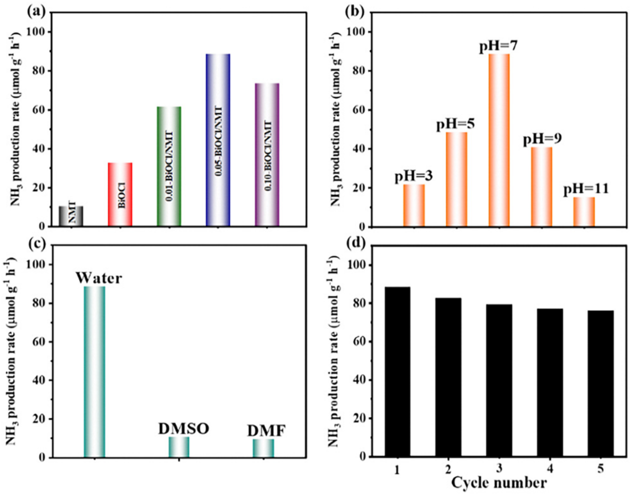

Fig. 9 (a) N_2 reduction rates of NMT, BiOCl and BiOCl/NMT; NH_3 production rates of 0.05-BiOCl/NMT in (b) different pH and (c) non-hydrogen solvents; and (d) N_2 fixation performance in cyclic tests of 0.05-BiOCl/NMT.

effectively promoted the separation efficiency of photogenerated carriers.[39] Suitable BiOCl loading was an essential factor affecting the catalytic activity of BiOCl/NMT. The PL spectra similarly indicated the excellent photogenerated carrier separation of the synthesized BiOCl/NMT, as shown in Fig. 8b. In contrast to pristine BiOCl and NMT, 0.05-BiOCl/NMT showed remarkably low PL intensity. A low signal peak represented that 0.05-BiOCl/NMT had a low carrier complexation rate. The electronic structure of semiconductors strongly influenced the kinetics of photogenerated electron–hole interactions.[40] The low PL intensity meant that a favorable contact area was formed at the interface of BiOCl and NMT. Energy level matching in heterojunction catalysts promoted rapid carrier separation and suppressed complexation.

Electrochemical impedance testing was performed to detect the resistance to photogenerated carrier migration to the catalyst surface. In the Nyquist spectrum (Fig. S8, ESI†), the arc radius of NMT was significantly larger than that of 0.05-BiOCl/NMT. This indicated that the photogenerated electrons were able to migrate between the interfaces of different semiconductors. The light absorption properties and multi-exciton effect of nanoscale quantum dots BiOCl yielded multiple beneficial effects.[41] The 0.05-BiOCl/NMT possessed the smallest arc radius under light energy radiation. The probability of photogenerated carriers recombining inside the catalyst was reduced, and the photoconversion efficiency was enhanced. The conductivity of 0.05-BiOCl/NMT under light energy was better, and the elevated concentration of OVs in BiOCl could capture more electrons to promote the separation of electrons and holes.

The photocatalytic nitrogen fixation activity of the synthesized samples was studied without the addition of any sacrificial reagent. Light emitted from a 300 W xenon lamp was chosen as the light source for the simulated catalytic experiments. After the formation of heterojunctions between NMT and BiOCl quantum dots, the nitrogen fixation activity of BiOCl/NMT remarkably elevated (Fig. 9a). The small sized BiOCl quantum dots exhibited abundant OVs at the edges of the structure, and these defective structures existed at the interface between BiOCl and NMT. More OVs were generated under photoinitiation, and the defect structures induced changes in the interfacial microenvironment and the local electronic structure.[42] The additional OVs in BiOCl could promote the adsorption of reactants by the catalyst and store photogenerated electrons to inhibit electron–hole recombination. 0.05-BiOCl/NMT expressed optimal nitrogen reduction performance along with the NH_3 generation at a rate of 88.6 μmol g^{-1} h^{-1}. The nitrogen fixation rate of 0.05-BiOCl/NMT was 8.5 and 2.7 times higher than that of BiOCl and NMT. The NH_3 generation rate for 0.10-BiOCl/NMT was 73.4 μmol g^{-1} h^{-1}. The photocatalytic activity of the composite system was enhanced with the increase of BiOCl loading. The OVs in BiOCl contributed to the adsorption of reactant N_2 and inhibited the electron–hole pair complexation. But excessive loading of BiOCl affected the rate of ammonia production, probably due to the fact that excess BiOCl hindered the absorption of light energy by the ligand in NMT. The high concentration of OVs in BiOCl may become a complex center for photoexcited electrons and holes, and the lifetime and effectiveness of photogenerated carriers were reduced. In addition, the electrochemical impedance and photocurrent intensity test results illustrated the optimal photocatalytic nitrogen fixation potential of 0.05-BiOCl/NMT. To illustrate the importance of OVs in BiOCl, we prepared BiOCl without OVs (WO-BiOCl) by referring to the synthesis method in the literature.[30] And 0.05-WO-BiOCl/NMT was synthesized according to a similar method, which had an ammonia synthesis rate of only 42.7 μmol g^{-1} h^{-1}. The controlled experimental data indicated that OVs in BiOCl played a crucial role in photocatalysis. Comparing our work with some existing literature in the field of photocatalytic nitrogen fixation (Table S1, ESI†), the synthesized Z-scheme heterojunction BiOCl/NMT showed a high ammonia generation rate. The enhanced BEF and fast carrier migration rate in BiOCl/NMT served as an important basis to ensure the efficient synthesis of ammonia. A controlled experiment on the nitrogen fixation activity of 0.05-BiOCl/NMT was performed with Nessler's assay, and the results of the test are shown in Table S2 (ESI†). The values obtained by the two test methods were close to each other.

The conversion of nitrogen to ammonia was associated with a multistep proton-coupled electron transfer, and control experiments to investigate the rate of ammonia production were completed under different pH conditions (Fig. 9b). In acidic environments at pH 3 or 5, the structures of NMT and BiOCl tended to be disrupted leading to a significant decrease in ammonia production rate of 0.05-BiOCl/NMT. In addition, high proton concentrations caused an inhibitory impact on the oxidation of water, which was similarly detrimental to ammonia production.[43] Under alkaline conditions, the insufficient concentration of protons severely impacted the hydrogenation process of $^*N_2$ either by distal or alternating mechanisms. Hence, an environment with a neutral pH was suitable for ammonia production. To further validate the necessity of protons for the photocatalytic nitrogen fixation reaction, the non-protonic solvents dimethyl sulfoxide (DMSO) and DMF were replaced with water as solvents. In Fig. 9c, the efficiency of nitrogen fixation was significantly affected in solutions which could not produce a hydrogen source. This suggested that water was the proton source in the nitrogen fixation process. In addition, we researched the nitrogen fixation activity under conditions of light radiation in an Ar atmosphere or under darkness in an N_2 environment. As shown in Fig. S9 (ESI†), ammonia production was negligible for each sample under both test conditions. Protons, light and N_2 were essential in the photocatalytic nitrogen fixation process. The source of nitrogen in the product NH_3 was explained by isotope labeling experiments, as shown in Fig. S10 (ESI†). $^{14}N_2$ and $^{15}N_2$ were passed into the catalytic device as feed gases, and different signal peaks appeared in the ^1H nuclear magnetic resonance (NMR) spectra. The control experiment indicated that the N in the catalytic product NH_3 originated from the reduction of the feed gas.

Cycling experiments were undertaken to illustrate the stability of the catalysts. After five cycles of testing, 0.05-BiOCl/NMT still manifested promising nitrogen fixation performance. In Fig. 9d, the ammonia production rate decreased from 88.6 to 76.1 μmol g^{-1} h^{-1}. The catalyst was repeatedly collected and dried during the cycle test. Inevitably, a small amount of catalyst was lost during the operation. As a result, the photocatalytic nitrogen fixation rate of 0.05-BiOCl/NMT exhibited a decreasing trend in the cycle test. In the previous data analysis, we observed that new OVs formed on the surface of A-0.05-BiOCl/NMT. The A-0.05-BiOCl/NMT placed in air for a long period of time was observed with the assistance of characterization methods, and no significant changes in the lattice parameters and microscopic morphology of the catalyst were detected (Fig. S11 and S12, ESI†). The ESR test result revealed that A-0.05-BiOCl/NMT was exposed to air for a long time, in which the intensity of the signal peaks of the OVs was weakened (Fig. S13, ESI†). 0.05-BiOCl/NMT still largely maintained its initial morphological features after photocatalytic nitrogen fixation, and the added OVs in A-0.05-BiOCl/NMT were unstable in air. A-0.05-BiOCl/NMT could be oxidized to 0.05-BiOCl/NMT in air for a period of time.

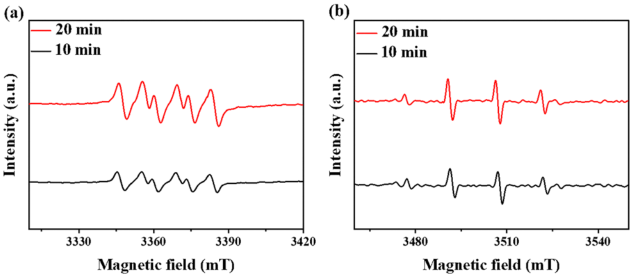

Fig. 10 EPR spectra of (a) $^{\bullet}O_2^-$ and (b) $^{\bullet}OH$ radicals for 0.05-BiOCl/NMT under light.

Active species capture experiments were performed to account for free radical species in the photocatalytic process, as shown in Fig. S14 (ESI†). The nitrogen fixation process may produce $^{\bullet}O_2^-$, h^+, and $^{\bullet}OH$, which were scavenged with benzoquinone (BQ), ethylene diamine tetraacetic acid (EDTA), and isopropanol (IPA), respectively.[44] From the test data, it was noticed that the three reagents affected the nitrogen fixation performance to different degrees. The order of influence of active species on N_2 reduction was $^{\bullet}O_2^- > {}^{\bullet}OH > h^+$. The main active species produced by 0.05-BiOCl/NMT were $^{\bullet}OH$ and $^{\bullet}O_2^-$ during photocatalytic nitrogen fixation. The radical species yielded by 0.05-BiOCl/NMT were further analyzed by ESR spectra, and 5,5-dimethyl-1-pyrroline-*N*-oxide (DMPO) acted as a spin trapping agent. Signal peaks associated with DMPO–$^{\bullet}O_2^-$ and DMPO–$^{\bullet}OH$ appeared in 0.05-BiOCl/NMT (Fig. 10). The intensity of the signal peaks was significantly increased with the prolongation of light irradiation. Light radiation modified the concentration of OVs in BiOCl, and rapid migration of electrons and holes occurred in 0.05-BiOCl/NMT to promote the production of $^{\bullet}OH$ and $^{\bullet}O_2^-$.

For clarifying the migration direction of photogenerated electrons at the interface of BiOCl and NMT, we probed the work functions (Φ) of both samples by the UPS test as shown in Fig. 11 and Fig. S15 (ESI†). Based on the formula of the work functions, the Φ values of NMT, BiOCl and A-BiOCl were 7.77, 8.87 and 9.32 eV, respectively.[45] The values of E_f for NMT, BiOCl and A-BiOCl of −7.77, −8.87 and −9.32 eV were acquired through the conversion relation between the E_f and the work function. The E_f positions underwent a downward migration with the increase of OVs in A-BiOCl. The test data directly indicated an increase in the E_f difference between NMT and A-BiOCl. The different work functions of NMT and BiOCl would lead to differences in their E_f levels. This resulted in the formation of electron density differences between NMT and

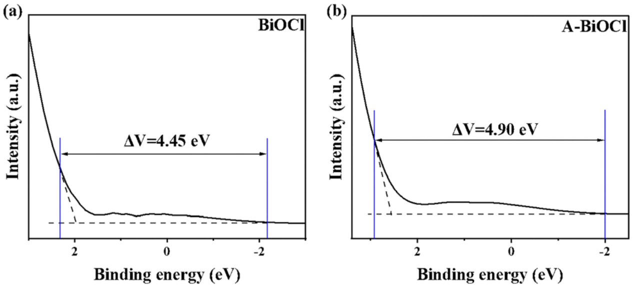

Fig. 11 UPS spectra of (a) BiOCl and (b) A-BiOCl.

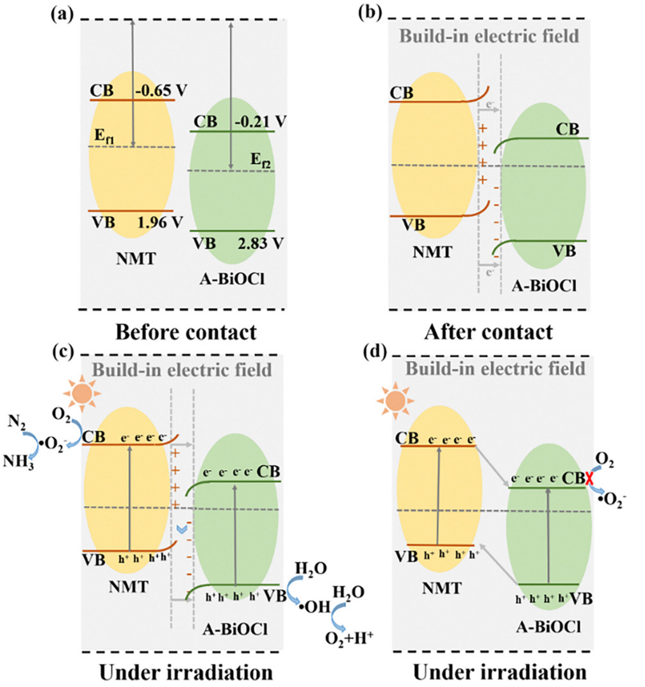

Fig. 12 Carrier migration mechanism and possible nitrogen fixation mechanism in 0.05-BiOCl/NMT.

BiOCl.[46] After being constructed as heterojunction catalysts, the E_f would reach a state of equilibrium after the formation of interfacial contact between BiOCl and NMT (Fig. 12). Since the E_f value of BiOCl was more negative than that of NMT, a BEF was formed between the two samples pointing from NMT to BiOCl.[47] The electrons in NMT would migrate to the surface of BiOCl after the formation of an interfacial contact. Thus, the E_f values of BiOCl and NMT were overlapped. The NMT was bended upward in its energy band due to the loss of electrons to form an electron depletion region. In contrast, BiOCl was an electron accumulating region due to the acquisition of electrons, and its energy bands underwent a downward bending.[48] The formed interfacial electric field suppressed the sustained electron transfer from NMT to BiOCl. Both electrons and holes were produced in the semiconductor material under the excitation of light energy. By the common effect of energy band bending and electric field force, the holes in NMT combined with the electrons in BiOCl. Since A-BiOCl exhibited a lower Fermi energy level, a stronger BEF between A-BiOCl and NMT was formed to promote rapid carrier migration between the interfaces.[49] A Z-scheme heterojunction was established between NMT and A-BiOCl, electrons and holes with strong redox potentials could facilitate the smooth progress of catalytic reactions. The OVs in BiOCl were tunable by light to enhance the BEF intensity between it and NMT, which enabled the rapid separation and migration of photogenerated carriers.

The reaction mechanism of BiOCl/NMT photocatalytic nitrogen fixation was proposed based on the above test results. The energy band relationship between NMT and BiOCl was feasible for the construction of Z-scheme heterojunctions. Under the radiation of light energy, photogenerated electrons and holes were generated simultaneously in NMT and BiOCl. According to the carrier migration mechanism of Z-scheme heterojunctions, the electrons in the CB of BiOCl migrated to the VB of NMT. The content of OVs in BiOCl quantum dots increased under the effect of light, and its E_f downward migration enhanced the BEF intensity between NMT and BiOCl. The optimization of a BEF promoted the transport of photogenerated carriers at the interface of NMT and BiOCl. If the electrons on the CB of the NMT migrated toward the CB of BiOCl (Fig. 12d), the energy level position of the CB of BiOCl did not satisfy the conditions for $^•O_2^-$ generation ($E(O_2/^•O_2^-)$ = −0.33 V *vs.* NHE). Ultrasmall-sized quantum dots resulted in the creation of defective structures on the BiOCl surface. In addition, the radiation of light caused additional OVs to be produced in BiOCl. The formed OVs boosted the adsorption of N_2 by the catalysts. The adsorbed N_2 could be reduced by $^•O_2^-$ and progressively hydrogenated by combining with protons to finally produce NH_3. Meanwhile, the holes on the VB of BiOCl had a strong oxidizing ability to oxidize water to $^•OH$, which further promoted N_2 reduction. The Z-scheme heterojunction BiOCl/NMT with an adjustable BEF not only contributed to the separation efficiency of photogenerated carriers, but also realized efficient nitrogen reduction.

The reaction mechanism of BiOCl/NMT photocatalytic nitrogen fixation was proposed based on the above test results. The energy band relationship between NMT and BiOCl was feasible for the construction of Z-scheme heterojunctions. Under the radiation of light energy, photogenerated electrons and holes were generated simultaneously in NMT and BiOCl. According to the carrier migration mechanism of Z-scheme heterojunctions, the electrons in the CB of BiOCl migrated to the VB of NMT. The retained photogenerated h^+ could oxidize water to form O_2 and protons. Photogenerated electrons were concentrated on the CB of the NMT, and had sufficient reducing energy (−0.65 V) to allow O_2 to be reduced to $^•O_2^-$ ($E(O_2/^•O_2^-)$ = −0.33 V *vs.* NHE). The content of OVs in BiOCl quantum dots increased under the effect of light, and its E_f downward migration enhanced the BEF intensity between NMT and BiOCl. The optimization of the BEF promoted the transport of photogenerated carriers at the interface of NMT and BiOCl. If the electrons on the CB of the NMT migrated toward the CB of BiOCl (Fig. 12d), the energy level position of the CB of BiOCl (−0.21 V) did not satisfy the conditions for $^•O_2^-$ generation. Ultrasmall-sized quantum dots resulted in the creation of defective structures on the BiOCl surface. In addition, the radiation of light caused additional OVs to be produced in BiOCl. The formed OVs boosted the adsorption of N_2 by the catalysts. The adsorbed N_2 could be reduced by $^•O_2^-$ and progressively hydrogenated by combining with protons to finally produce NH_3. Meanwhile, the holes on the VB of BiOCl had a strong oxidizing ability to oxidize water to $^•OH$, which further promoted N_2 reduction. The Z-scheme heterojunction BiOCl/NMT with an adjustable BEF not only contributed to the separation efficiency of photogenerated carriers, but also realized efficient nitrogen reduction.

4. Conclusions

In summary, a BiOCl/NMT Z-scheme heterojunction was constructed through a solvothermal process and adsorption–deposition methods. Under photoinitiation, BiOCl quantum dots could be transformed into defective structures with more OVs. Increasing the concentration of defect structures in BiOCl not only altered the energy band structure, but also further modulated the position of the Fermi energy level. Since A-BiOCl exhibited a lower E_f, a stronger BEF between A-BiOCl and NMT was formed to promote rapid carrier migration between the interfaces. Signal peaks associated with DMPO–$^{\bullet}O_2^-$ and DMPO–$^{\bullet}$OH appeared in 0.05-BiOCl/NMT. The intensity of the signal peaks significantly increased with the prolongation of light irradiation. This might be related to the increased content of OVs in BiOCl, which facilitated the formation of reactive free radicals. 0.05-BiOCl/NMT expressed optimal nitrogen reduction performance along with NH_3 generation at a rate of 88.6 μmol g^{-1} h^{-1}. The nitrogen fixation rate of 0.05-BiOCl/NMT was 8.5 and 2.7 times higher than that of BiOCl and NMT. This work adjusted the BEF intensity by a straightforward self-conversion to a defective structure, which offered fresh insights into the promotion of carrier separation in photocatalytic nitrogen fixation. Photocatalytic nitrogen fixation was characterized by low cost, low energy consumption and environmental friendliness, and it provided a new development direction for industrial ammonia synthesis.

Conflicts of interest

There are no conflicts to declare.

Data availability

The data supporting this article have been included as part of the ESI.†

Acknowledgements

The project was supported by the Science and Technology Development Project of Jilin Province (YDZJ202501ZYTS386) and the University level research project of Jilin Engineering and Normal University (Grant No. BSKJ202302).

Notes and references

1 S. C. Zhang, H. Hong, R. Zhang, Z. Q. Wei, Y. Q. Wang, D. Chen, C. Li, P. Li, H. L. Cui, Y. Hou, S. N. Wang, J. C. Ho, Y. Guo, Z. D. Huang and C. Y. Zhi, *Angew. Chem., Int. Ed.*, 2025, **64**, e2024128.

2 X. Y. Lu, J. D. Hu, X. H. Jiang, J. H. Li, Z. J. Lu, J. Xie and Y. L. Cao, *Adv. Funct. Mater.*, 2025, 2502690.

3 K. Cheng, S. B. Li, Q. Y. Cheng, L. Zhang, Y. F. Jiang, F. B. Li, H. Y. Ma and D. Q. Zhang, *Adv. Funct. Mater.*, 2025, **35**, 2417914.

4 Y. X. Chang, L. H. Lin, J. L. Shen, Z. Lin, X. Y. Deng, W. M. Sun, X. Y. Wu, Y. F. Wang, Y. Q. Li and Z. M. Xu, *J. Hazard. Mater.*, 2025, **481**, 136588.

5 M. Sharma, A. Kumar, D. Sajwan, K. Kumari, B. P. Mishra and V. Krishnan, *Adv. Sustainable Syst.*, 2025, **9**, 2400903.

6 D. H. Cui, X. Yang, Y. Liu, T. Ou, Xi. Y. Kong, Y. L. Zhang, J. W. Zhang and F. Y. Li, *J. Colloid Interface Sci.*, 2025, **678**, 955.

7 Z. Zhong, H. J. Zhang, Y. Y. Yang, T. K. Zhang, X. H. Qu, L. Ma, H. L. Cao, Y. D. D. Hou and J. Lü, *ACS Catal.*, 2025, **15**, 6334.

8 T. Q. Wang, R. Zhai, Z. Y. Liu, S. Y. Liu, Y. H. Cheng and J. Y. Zhang, *J. Mater. Chem. A*, 2025, **13**, 13551–13559.

9 J. X. Liu, Z. Li, L. Nie, X. X. Xue and M. Liu, *Sep. Purif. Technol.*, 2025, **354**, 128882.

10 Y. Q. Liu, Y. H. Shi, X. Xin, Z. F. Zhao, J. D. Tan, D. Yang and Z. Y. Jiang, *Appl. Catal., B*, 2025, **363**, 124815.

11 P. Priyadarshini, A. Mishra, S. Nayak and K. Parida, *Nanoscale*, 2025, **17**, 4906.

12 W. H. Deng, M. Y. Zhang, C. S. Li, M. S. Yao and G. Xu, *Angew. Chem., Int. Ed.*, 2025, **64**, e202419195.

13 Y. Li, X. Y. Yang, M. Y. Wang, D. Y. Yue, J. Wu and H. J. Song, *Sep. Purif. Technol.*, 2025, **361**, 131567.

14 J. P. Zhao, Y. F. Ma, Z. M. Tong, M. Wang, L. T. Xiao, S. T. Jia and X. Y. Chen, *J. Environ. Chem. Eng.*, 2025, **13**, 115693.

15 Y. Tian, R. Hai, Y. X. Liu, D. Y. Nie, Y. T. Lu, H. X. Zhu and X. Yang, *ACS Appl. Mater. Interfaces*, 2025, **17**, 30988–30999.

16 Y. Liu, D. H. Cui, X. Yang and F. Y. Li, *Inorg. Chem. Front.*, 2025, **12**, 3438.

17 X. Y. Chu, S. K. Liu, B. B. Luan, Y. Zhang, Y. M. Xi, L. H. Shao, F. M. Zhang and Y. Q. Lan, *Angew. Chem., Int. Ed.*, 2025, **64**, e202422940.

18 H. P. Jiang, L. L. Wang, X. H. Yu, L. J. Sun, J. H. Li, J. Yang and Q. Q. Li, *Chem. Eng. J.*, 2023, **466**, 143129.

19 S. Zhao, Y. Y. Wan, L. Han, B. C. Tian, Z. Y. Duan, R. D. Su and X. B. Li, *Carbon Lett.*, 2025, **35**, 287.

20 M. Rezaei, A. Nezamzadeh-Ejhieh and A. R. Massah, *Mater. Today Energy*, 2025, **48**, 101754.

21 X. Zhang, M. Zhang, C. Luo, Y. M. Li, L. L. Zhang, C. Li, X. D. Zhang, J. J. Liao and W. Zhou, *Appl. Catal., B*, 2025, **371**, 125288.

22 H. L. Shi, M. J. Xu, C. Yy Leng, L. L. Ai, L. X. Wang, H. Fan and S. M. Wu, *J. Colloid Interface Sci.*, 2025, **680**, 1067.

23 S. J. Wang, D. X. Song, L. J. Liao, M. X. Li, Z. Z. Li and W. Zhou, *Adv. Colloid Interface Sci.*, 2024, **324**, 103088.

24 T. T. Hu, P. P. Feng, H. Q. Chu, X. P. Wang, F. S. Liu and W. Zhou, *Adv. Funct. Mater.*, 2025, **35**, 2416556.

25 C. Z. Zhu, Q. H. Tian, S. P. Wan, H. T. Xu, J. G. Hu and L. Q. Jing, *Chem. Eng. J.*, 2024, **497**, 154689.

26 J. R. Tian, Z. X. Zhao, H. Q. Ling, Z. Qq Zhang, H. Ablat and X. Nurmamat, *Int. J. Hydrogen Energy*, 2024, **87**, 686.

27 N. Wang, W. Ma and Y. Jin, *Mater. Res. Express*, 2024, **11**, 075506.

28 R. F. Yan, S. S. Zhi, M. M. Hao, Y. L. Liu, H. J. Wang, S. L. Zhou, K. Jiang and D. P. Wu, *Chemosphere*, 2025, **370**, 143935.

29 N. Y. Lim, S. L. Chiam, C. P. Leo, S. Y. Pung, C. K. Chang and W. L. Ang, *Int. J. Biol. Macromol.*, 2025, **308**, 142421.

30 Y. Zhong, C. L. Wu, Y. M. Feng, D. M. Chen, Y. X. Wang, D. Hao and H. Ding, *Appl. Surf. Sci.*, 2022, **585**, 152656.

31 J. Farahbakhsh, M. Golgoli, M. Najafi, S. Z. Haeri, M. Khiadani, A. Razmjou and M. Zargar, *Sep. Purif. Technol.*, 2025, **353**, 128273.

32 S. J. Shah, X. Q. Luan, X. Yu, W. G. Su, Y. C. Wang, Z. X. Zhao and Z. X. Zhao, *J. Colloid Interface Sci.*, 2024, **663**, 491.

33 Z. X. Wang, F. Xiang, C. Chen, J. Wang, X. C. Ma, X. Zhao and W. L. Fan, *J. Catal.*, 2025, **447**, 116112.

34 M. X. Cheng, H. L. Li, Z. Y. Wu, Z. X. Yu, X. M. Tao and L. Huang, *Sep. Purif. Technol.*, 2025, **354**, 129299.

35 F. F. Lang, L. L. Zhang, Y. Li, X. J. Xi, J. D. Pang, W. J. Zheng, H. C. Zhou and X. H. Bu, *Angew. Chem., Int. Ed.*, 2025, **137**, e202422517.

36 Z. Y. Jiang, H. Li, Z. M. Yuan, Z. Wang, M. H. Fan, W. K. Miao and H. He, *J. Environ. Sci.*, 2024, **140**, 37.

37 J. Di, C. Chen, Y. Wu, H. Chen, J. Xiong, R. Long, S. Z. Li, L. Song, W. Jiang and Z. Liu, *Adv. Mater.*, 2024, **36**, 2401914.

38 P. H. M. Andrade, C. Volkringer, T. Loiseau, A. Tejeda, M. Hureau and A. Moissette, *Appl. Mater. Today*, 2024, **37**, 102094.

39 Y. Li, Y. M. Huang, H. H. Zhang, X. L. Wang, L. L. Gao, Y. Zhang, Y. F. Liao, J. Y. Meng, Y. Y. Cui and W. L. Dai, *Appl. Catal., B*, 2025, **361**, 124657.

40 M. Bilal, M. Q. Alfaifi, S. B. Ahmed, M. M. Abduljawad, Y. I. Alrashed, E. S. Aldurahim and Y. A. Alassmy, *Mater. Sci. Semicond. Process.*, 2025, **186**, 109051.

41 P. K. Li, R. J. Wu, P. S. Li, S. Gao, Z. P. Qin, X. J. Song, W. M. Sun, Z. R. Hua, Q. Wang and S. W. Chen, *Adv. Sci.*, 2024, **11**, 2408829.

42 H. L. Tong, J. N. Zhang, B. M. Sun, H. Shi, N. Q. Ren, S. J. You and G. S. Zhang, *Environ. Res.*, 2025, **275**, 121412.

43 K. Pournemati, A. Habibi-Yangjeh and A. Khataee, *ACS Appl. Nano Mater.*, 2024, **7**, 2200–2213.

44 C. J. Zheng, R. C. Zhang, K. Xu, J. Zhang, K. Wang, W. Chen, G. B. Huang and H. F. Yin, *Carbon*, 2024, **226**, 119153.

45 E. Z. Deng, Y. Z. Fan, H. P. Wang, Y. Y. Li, C. Peng and J. W. Liu, *Inorg. Chem.*, 2024, **63**, 1449.

46 S. M. Ghoreishian, K. S. Ranjith, M. Ghasemi, B. Park, S. K. Hwang, N. Irannejad, M. Norouzi, S. Y. Park, R. Behjatmanesh-Ardakani, S. M. Pourmortazavi, S. Mirsadeghi, Y. K. Han and Y. S. Huh, *Chem. Eng. J.*, 2023, **452**, 139435.

47 S. M. Ghoreishian, K. S. Ranjith, B. Park, S. K. Hwang, R. Hosseini, R. Behjatmanesh-Ardakani, S. M. Pourmortazavi, H. U. Lee, B. Son, S. Mirsadeghi, Y. K. Han and Y. S. Huh, *Chem. Eng. J.*, 2021, **419**, 129530.

48 Y. Liu, D. H. Cui, T. T. Zhang, X. Yang, C. X. Wang and F. Y. Li, *Chem. Eng. J.*, 2024, **497**, 154416.

49 H. Guo, W. X. Chen, X. Q. Qiao, C. Li, B. J. Sun, D. F. Hou, M. D. Wang, X. Q. Wu, T. Wu, R. Chi and D. S. Li, *Nano Energy*, 2025, **135**, 110672.